Near-Field Aeroacoustic Shape Optimization at Low Reynolds Numbers

Mohsen Hamedi^{*} and Brian Vermeire[‡] Concordia University, Montreal, Quebec H3G 1M8, Canada

https://doi.org/10.2514/1.J063650

We investigate the feasibility of gradient-free aeroacoustic shape optimization using the flux reconstruction (FR) approach to study two-dimensional flow at low Reynolds numbers. The overall sound pressure level (OASPL) is computed via the direct acoustic approach, and optimization is performed using the gradient-free mesh adaptive direct search (MADS) algorithm. The proposed framework is assessed across three problems. First, flow over an open cavity is investigated at a Reynolds number of Re = 1500 and freestream Mach number of $M_{\infty} = 0.15$, resulting in a 7.9 dB noise reduction. The second case considers tandem cylinders at Re = 200 and $M_{\infty} = 0.2$, achieving a 16.5 dB noise reduction by optimizing the distance between the cylinders and their diameter ratio. Finally, a NACA0012 airfoil is optimized at Re = 10,000 and $M_{\infty} = 0.2$ to reduce trailing edge noise. The airfoil's shape is optimized to generate a new four-digit NACA airfoil at an appropriate angle of attack to reduce OASPL while maintaining the baseline time-averaged lift coefficient and preventing an increase in the baseline time-averaged drag coefficient. The optimized airfoil is silent at 0 dB and the drag coefficient is decreased by 24.95%. These results demonstrate the feasibility of shape optimization using MADS and FR for aeroacoustic design.

A. Governing Equations

The compressible unsteady Navier–Stokes equations can be cast in the following general form:

$$\frac{\partial \mathbf{u}}{\partial t} + \nabla \cdot \mathbf{F} = 0 \tag{1}$$

where t is time and u is a vector of conserved variables:

$$\boldsymbol{u} = \begin{bmatrix} \rho \\ \rho u_i \\ \rho E \end{bmatrix} \tag{2}$$

where ρ is density, ρu_i is a component of the momentum, u_i are velocity components, and ρE is the total energy. The inviscid and viscous Navier–Stokes fluxes are

$$\boldsymbol{F}_{i,j}(\boldsymbol{u}) = \begin{bmatrix} \rho u_j \\ \rho u_i u_j + \delta_{ij} p \\ u_j (\rho E + p) \end{bmatrix}$$
(3)

and

$$\mathbf{F}_{\nu,j}(\mathbf{u}, \nabla \mathbf{u}) = \begin{bmatrix} 0 \\ \tau_{ij} \\ -q_j - u_i \tau_{ij} \end{bmatrix}$$
(4)

respectively, where δ_{ij} is the Kronecker delta. The pressure is determined via the ideal gas law as

$$p = (\gamma - 1)\rho \left(E - \frac{1}{2}u_k u_k\right) \tag{5}$$

where $\gamma = 1.4$ is the ratio of the specific heat at constant pressure, c_p , to the specific heat at constant volume c_p . The viscous stress tensor is

$$\tau_{ij} = \mu \left(\frac{\partial u_i}{\partial x_j} + \frac{\partial u_j}{\partial x_i} - \frac{2}{3} \frac{\partial u_k}{\partial x_k} \delta_{ij} \right)$$
 (6)

and the heat flux is

$$q_{j} = -\frac{\mu}{Pr} \frac{\partial}{\partial x_{j}} \left(E + \frac{p}{\rho} - \frac{1}{2} u_{k} u_{k} \right) \tag{7}$$

where μ is the dynamic viscosity and Pr=0.71 is the Prandtl number.

B. Flux Reconstruction

The FR approach [7] discretizes the divergence operator for general advection—diffusion equations of the form shown in Eq. (1). Known for its high-order accuracy, generality, robustness, and compatibility with modern hardware architectures [11], FR offers superior accuracy with fewer degrees of freedom and reduced computational cost compared to conventional low-order methods [31]. Its suitability extends to scale-resolving simulations, where its numerical error behavior is leveraged for implicit large eddy simulation (ILES) [32], and via filtering approaches for highly underresolved problems [33]. The FR framework is outlined here in multiple dimensions, following Wang's formulation [34].

In the FR approach, the computational domain Ω is discretized into a mesh of N_e non-overlapping elements such that

$$\Omega = \bigcup_{k=1}^{N_e} \Omega_k, \qquad \bigcap_{k=1}^{N_e} \Omega_k = \emptyset$$
 (8)

Each element Ω_k contains a number of solution points based on the desired solution polynomial degree. For the sake of simplicity, these elements are transformed from the physical space x to a standard reference space ξ , where x and ξ are the spatial coordinates in the physical and reference spaces, respectively. The transformation of these elements is done via an invertible mapping function M such that

$$x = M(\xi) \iff \xi = M^{-1}(x) \tag{9}$$

The Jacobian of this mapping can be found at any point from

$$J = \frac{\partial x}{\partial \xi} \tag{10}$$

which enables all element operations to be performed on the same reference element and, upon completion, mapped back to the physical locations.

In this study, the solution and flux points are located at tensor products of Gauss points for quadrilateral elements and Williams—Shunn points [35] for triangular elements, as depicted in Fig. 1. The solution is approximated at each solution point, and then the solution polynomial within each element is interpolated using nodal basis functions, ensuring elementwise continuity of the solution

$$\boldsymbol{u}_{k}^{\delta}(\boldsymbol{\xi},t) = \sum_{i=1}^{N_{p}} \boldsymbol{u}_{k,i}^{\delta} \phi_{i}(\boldsymbol{\xi})$$
 (11)

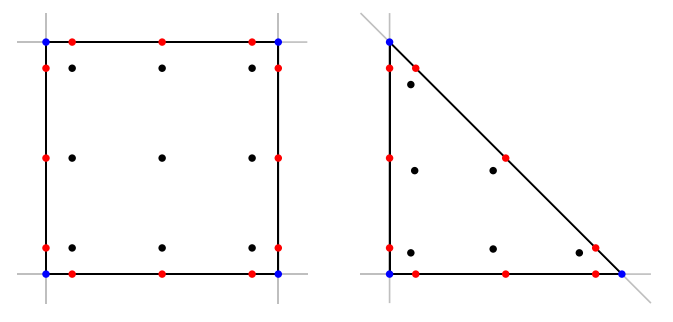
where $u_{k,i}^{\delta}$ is the numerical solution at point i within element Ω_k , N_p is the total number of solution points within the element Ω_k , and $\phi_i(\xi)$ is the nodal basis function at point i. Furthermore, the flux polynomial is interpolated using nodal basis functions

$$\boldsymbol{F}_{k}^{\delta D}(\boldsymbol{\xi},t) = \sum_{i=1}^{N_{p}} F_{k,i}^{\delta} \phi_{i}(\boldsymbol{\xi})$$
 (12)

where $F_{k,i}^\delta=f(U_{k,i}^\delta,\nabla U_{k,i}^\delta)$ is the numerical flux value at point i within element Ω_k . The constructed numerical flux function $F_k^{\delta D}(\xi,t)$ is allowed to be discontinuous across cell interfaces, and the superscript D denotes this discontinuity. Thus, a common Riemann flux must be defined to replace the normal flux. In this study, a Rusanov/Lax-Friedrichs flux is used at the interface between elements. To account for the jumps across cells, we follow Wang's formulation [34] for simplex elements. By defining a correction field, $\vartheta_k \in \mathbb{P}^{\mathcal{D}}$, Eq. (1) is rewritten within each element and must be satisfied at each solution point, i.e.,

$$\frac{d\boldsymbol{u}_{k,i}^{\delta}}{dt} + (\nabla \cdot \boldsymbol{F}_{k}^{\delta})_{\boldsymbol{\xi}_{k,i}} + \vartheta_{k,i} = 0$$
 (13)

The correction field ensures a globally continuous flux polynomial and can be determined for each solution point i, within element k, by



a) Quadrilateral element types

b) Triangular element types

Fig. 1 The computational element Ω_k , with solution points in black, flux points in red, and mapping points in blue, for a $\mathcal{P}2$ discretization.

(17)

$$\vartheta_{k,i} = \frac{1}{|\Omega_k|} \sum_{f \in \partial \Omega_k} \sum_j \alpha_{i,f,j} [\tilde{F}]_{f,j} S_f \tag{14}$$

where f denotes the faces of the element Ω_k , j is the index for flux points, $\alpha_{i,f,j}$ are constant lifting coefficients, $[\tilde{F}]_{f,j}$ is the difference between a common Riemann flux at point j and the value of the internal flux, and S_f is the area of the face f. The lifting coefficients are computed using a weighting function W and are independent of both geometry and the solution [34]. In this study, the DG method is recovered via the FR formulation by choosing nodal basis functions as the weighting function [34], and the Rusanov and second method of Bassi and Rebay (BR2) are used for the common inviscid and viscous flux.

C. Mesh Adaptive Direct Search Optimization

In this study, the MADS optimization technique is used, which falls between the generalized pattern search (GPS) [36] and the Coope and Price frame-based methods [37]. Unlike GPS, MADS allows for a more flexible exploration of the design space during the optimization process, which makes it a more effective solution for both unconstrained and linearly constrained optimization [21]. A major advantage of MADS over GPS is its flexible local exploration, known as poll directions, rather than a fixed set of directions. Two parameters are defined in the context of the MADS optimization: the mesh size parameter Δ^m and the poll size parameter Δ^p . The mesh size parameter determines the resolution of the design space mesh. A higher resolution leads to a more precise search, while a lower resolution allows for a wider search and a higher chance of finding the global optimal solution. The poll size parameter determines the neighborhood size around the incumbent point for selecting new trial points. The number of trial points per design cycle can be either n + 1, known as minimal positive basis, or 2n, known as maximal positive basis [21], where n is the number of design variables. In this study, the minimal positive basis construction is used.

The MADS algorithm consists of two sequential steps in each iteration: the search step and the poll step. Initially, the optimization procedure starts with the search step at the initial design point, $\mathcal{X}_0 = [\mathcal{X}_0^1, \mathcal{X}_0^2, \dots, \mathcal{X}_0^n]$, where the subscript is the optimization iteration and the superscript denotes each design parameter. Pseudo-random trial points are generated, and infeasible ones, which are points within the design space not meeting the optimization problem's constraints, are discarded. The trial points are generated based on the current mesh and the direction vectors, $d_j \in \mathcal{D}$ (for $j = 1, 2, \dots, n$), where \mathcal{D} is the design space. \mathcal{D} must be a positive spanning set [38], and each direction d_j must be the product of some fixed nonsingular generating matrix by an integer vector [21]. The mesh at iteration k is defined as [21]

$$\mathcal{M}_k = \bigcup_{\mathcal{X} \in \mathcal{S}_k} \{ \mathcal{X} + \Delta_k^m \mathcal{D}z : z \in \mathbb{N}^{n_{\mathcal{D}}} \}$$
 (15)

where \mathcal{S}_k is the set of trial points that the objective function is evaluated at, in iteration k. The mesh \mathcal{M}_k is constructed from a finite set of $n_{\mathcal{D}}$ directions, $\mathcal{D} \subset \mathbb{R}^n$, scaled by a mesh size parameter $\Delta_k^m \in \mathbb{R}_+$. The objective function is evaluated at these trial points. The iteration terminates either after evaluating the objective function at all trial points or upon finding a lower objective function, where the latter is employed in this study. Then, the next iteration starts with a new incumbent solution $\mathcal{X}_{k+1} \in \Omega$ with objective function of $\mathcal{F}(\mathcal{X}_{k+1}) < \mathcal{F}(\mathcal{X}_k)$, and a mesh size parameter $\Delta_{k+1}^m \geq \Delta_k^m$. The maximum value of the mesh size parameter, at any iteration, is set to one, $\Delta_{\max}^m = 1$. Note that the design space of each design variable is scaled to one, and a mesh size parameter of one can cover the entire design space.

On the other hand, if the search step fails to find a new optimum, the poll step is invoked before terminating the current optimization iteration. In the poll step, the mesh size parameter is reduced to define a new set of trial points closer to the incumbent design. The key

difference between GPS and MADS is the new poll size parameter, $\Delta_k^p \in \mathbb{R}_+$, that controls the magnitude of the distance between trial points generated by the poll step to the incumbent point. This new set of trial points defined in the poll step is called a frame. The MADS frame at iteration k is defined to be [21]

$$P_k = \{ \mathcal{X}_k + \Delta_k^m d : d \in \mathcal{D}_k \} \subset \mathcal{M}_k$$
 (16)

where \mathcal{D}_k is a positive spanning set. In each MADS iteration, the mesh and poll size parameters are defined. The mesh size parameter of the new iteration is defined as [21]

$$\Delta_{k+1}^{m} = \begin{cases} \frac{1}{4} \Delta_{k}^{m} & \text{if the search step fails to find an improved design point,} \\ 4\Delta_{k}^{m} & \text{if an improved design point is found, and if } \Delta_{k}^{m} \leq \frac{1}{4}, \\ \Delta_{k}^{m} & \text{otherwise} \end{cases}$$

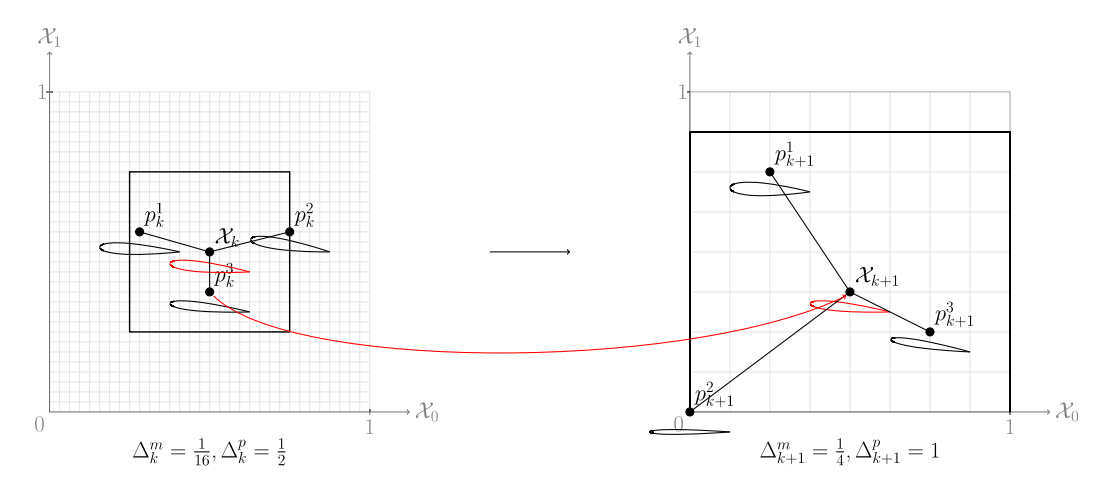
These rules ensure that Δ_k^m is always a power of 4 and never exceeds 1. The poll size parameter is also defined as [21]

$$\Delta_{k+1}^{p} = \begin{cases} n\sqrt{\Delta_{k}^{m}} & \text{if the minimal positive basis construction is used,} \\ \sqrt{\Delta_{k}^{m}} & \text{if the maximal positive basis construction is used} \end{cases}$$
(18)

As an example, which will be considered in detail in the numerical results section, consider a NACA four-digit airfoil where the design parameters are the airfoil's thickness $\mathcal{X}_1 \in [6, 20]$ and the angle of attack $\mathcal{X}_2 \in [0^\circ, 12^\circ]$. In this case, the bottom-left corner in the design space $[\mathcal{X}_1, \mathcal{X}_2] = [0, 0]$ shown in Fig. 2 corresponds to the minimum thickness and angle of attack. In contrast, the top-right corner $[\mathcal{X}_1, \mathcal{X}_2] = [1, 1]$ would correspond to the maximum thickness and angle of attack. Our objective is to find the point in the allowable design space that produces minimal noise. Starting from some initial design \mathcal{X}_0 and initial mesh and poll size parameters, we start by searching in the poll region at three candidate designs p_k^1 , p_k^2 , and p_k^3 . If, for example, p_k^3 is a configuration that produces less noise, we recenter our search around this point as our new optimal design, and increase the mesh size parameter for the subsequent step, as shown in Fig. 2a. However, if none of these points are quieter, we maintain the current optimal design, and shrink the mesh and poll size parameters for the subsequent step. This means that designs closer to the current optimum, i.e., more similar thickness and angle of attack, will be searched in the next step. Finally, when a new incumbent objective function is found in a design iteration, the optimization may converge or continue depending on the stopping criterion. The optimization problem is terminated when the stopping criteria are met.

III. Deep Cavity

Flow over a two-dimensional deep cavity is a classical problem in fluid mechanics and aeroacoustics and has been the subject of extensive research due to its relevance for a range of engineering applications. The flow over a cavity is characterized by a complex interplay between the boundary layer, the recirculation zone inside the cavity, and the external flow. The presence of the cavity can lead to a variety of aerodynamic and aeroacoustic phenomena, such as flow separation, unsteady vortex shedding, and acoustic resonance. Understanding the aerodynamic and aeroacoustic characteristics of flow over a cavity is crucial for optimizing the design and performance of many engineering systems. This topic has been studied using various techniques, including experiments [39], CFD simulations [40,41], and aeroacoustic analysis [42–44]. The geometry of a cavity is typically given in terms of the length-to-depth ratio, L/D, depicted in Fig. 3. The Reynolds



a) Search step

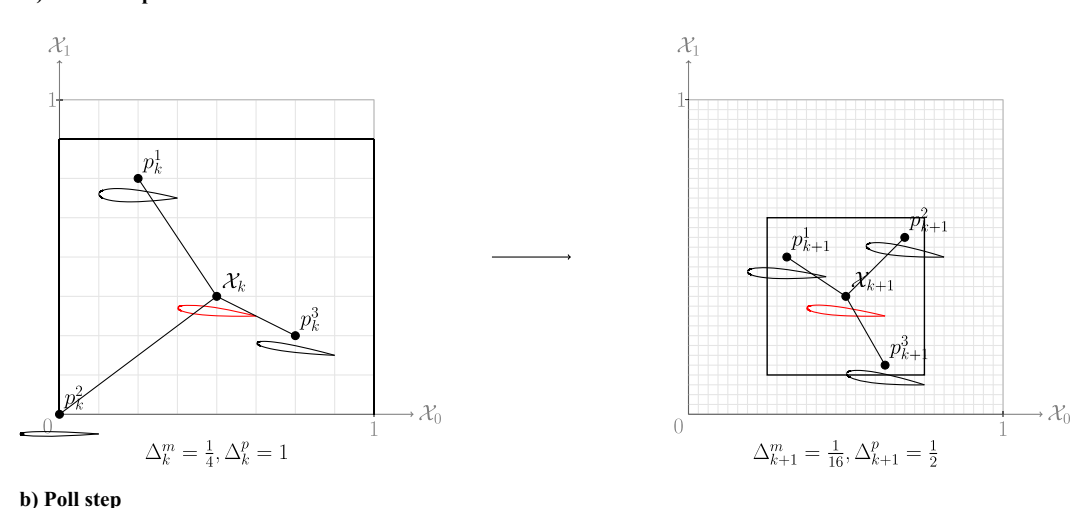


Fig. 2 Search and poll steps of the MADS optimization techniques for iteration k for the NACA example.



Fig. 3 The geometry of a two-dimensional cavity.

number is usually based on the depth of the cavity, $Re_D = U_\infty D/\nu$, where U_∞ is the freestream velocity and ν is the kinematic viscosity. The numerical simulation is first validated using the numerical reference study [42], and then the optimization procedure is explained.

A. Validation

In this section, the flow simulation over an open deep cavity is validated by comparing the time history of drag coefficient, pressure perturbation coefficient, and the OASPL at observer locations with the reference data [42].

1. Computational Details

The entrance length of the domain is set to 5D, which affects the oscillation regime significantly and results in a shear layer mode with the time-averaged boundary-layer thickness of $\delta \approx 0.3D$ at the cavity entrance. The outflow boundary is 80D away from the downstream cavity wall, where the last 50D of the downstream domain acts as a buffer region to eliminate the reflections of the acoustic waves from the computational boundaries. The resolved domain in the y direction extends between 0 < y/D < 20, and the buffer region extends between

20 < y/D < 40. Stretching ratios of 1.05 and 1.075 are used in the resolved and buffer regions, respectively, with the smallest element size of 0.05D inside the cavity. A total of 13,076 quadrangular elements are used to validate the open cavity with $\mathcal{P}2$, resulting in 117,684 solution points. The boundary conditions of the domain, along with the cavity's geometry and mesh, are shown in Fig. 4. The length-to-depth ratio of the cavity is L/D = 4, the Reynolds number based on the cavity depth is $Re_D = 1500$, and the inflow Mach number is $M_{\infty} = 0.15$.

2. Results and Discussion

The simulation is run for $100t_c$, where $t_c = D/U_\infty$ and U_∞ is the freestream velocity, to allow initial transients to disappear and the simulation to reach a fully developed behavior. The drag coefficient of the open cavity is defined as

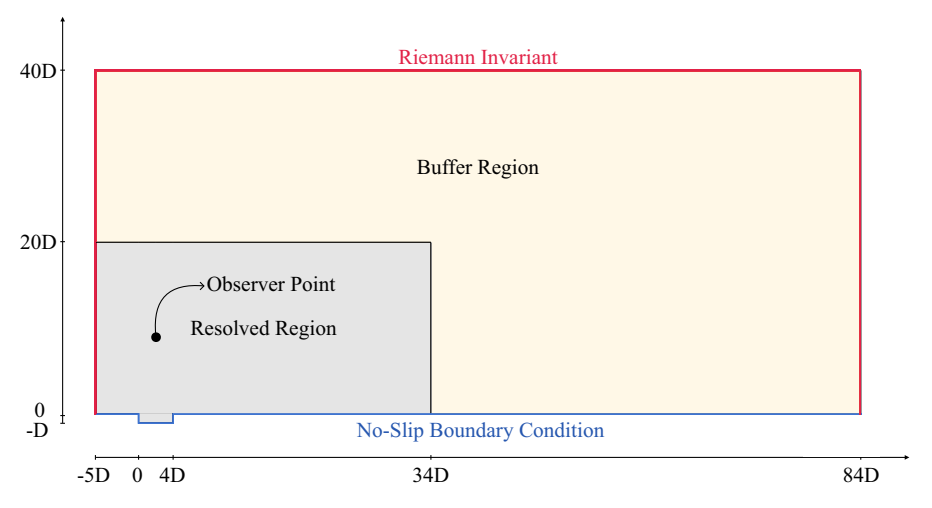
$$c_d = \frac{F_x}{(1/2)\rho_\infty U_\infty^2 D} \tag{19}$$

where ρ_{∞} is the freestream density and F_x is force per unit width in the x direction and is computed on the three cavity walls. The drag coefficient of the open cavity is plotted against the convective time in Fig. 5, which is in good agreement with the Ref. [42].

The pressure perturbation coefficient is defined as

$$c_p' = c_p - \overline{c_p} \tag{20}$$

where $\overline{c_p}$ is the time-averaged pressure coefficient, and c_p is the instantaneous pressure coefficient defined as



a) The geometry

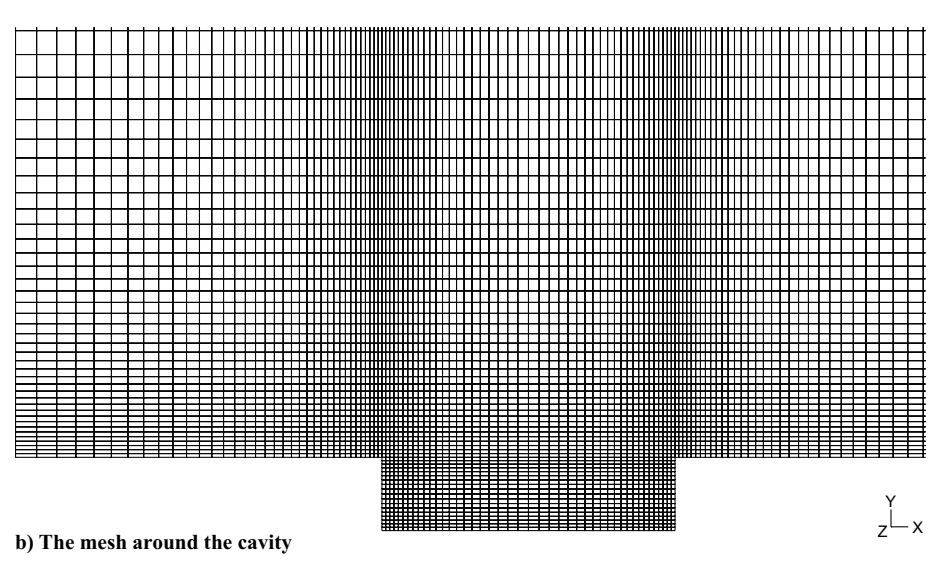


Fig. 4 The computational domain of the open cavity.

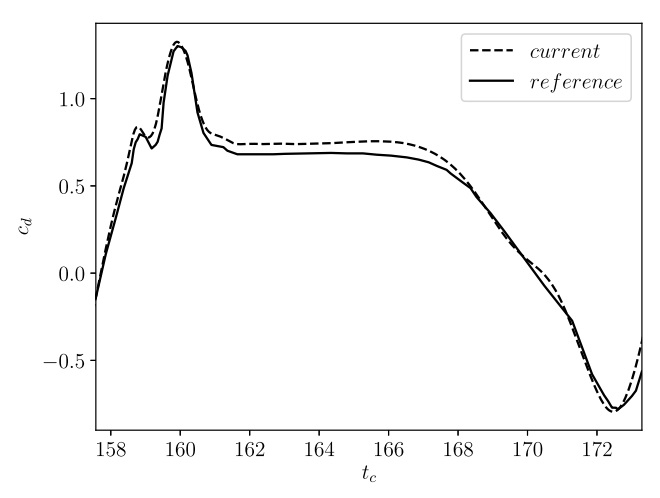


Fig. 5 The time history of drag coefficient of the open cavity.

$$c_p = \frac{p - p_{\infty}}{(1/2)\rho_{\infty}U_{\infty}^2} \tag{21}$$

where p is the static pressure, and p_{∞} is the freestream pressure. The c_p' is plotted against t_c for one convective time at an observer point located at [x/D=1, y/D=7.16] in Fig. 6. And, finally, the OASPL at a set of observer points is computed and shown

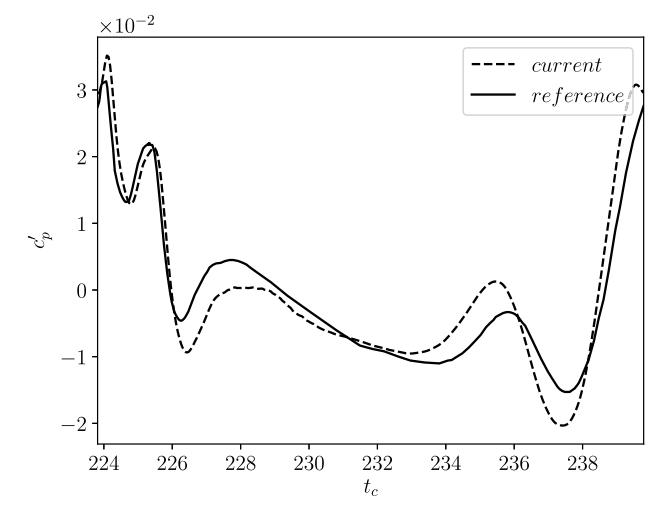


Fig. 6 The pressure perturbation coefficient of the open cavity at [x/D,y/D] = [1,7.16].

in Fig. 7, where excellent agreement with the reference results is observed near the trailing edge of the cavity. However, some minor discrepancies are observed at data points further upstream, which are also apparent in the time series of the pressure

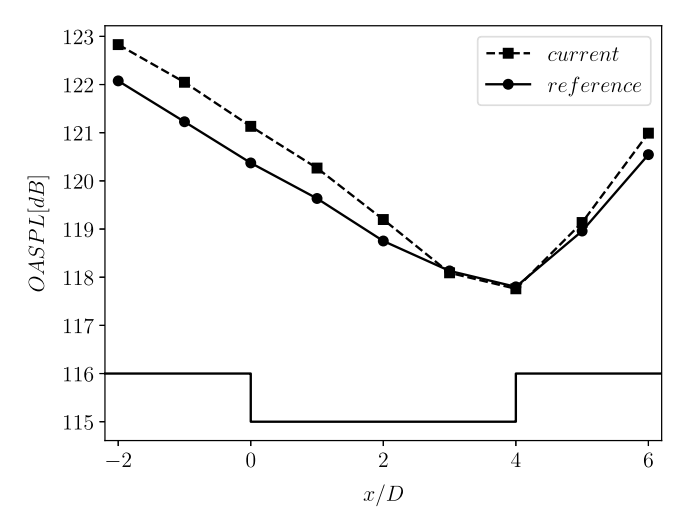


Fig. 7 The OASPL of the open cavity.

perturbation coefficient provided in Fig. $\underline{6}$. As noted in this prior work, the acoustics of open cavities are highly sensitive to the incoming boundary layer. Best efforts were made to match the mean velocity profiles provided in $[\underline{42}]$, but the available reference configuration is not precise enough to assess whether an exact match is obtained.

The periodicity of the flow can be described by the fundamental or Strouhal frequency, where St = 2.444 based on the length of the cavity, is in excellent agreement with the reported value of 2.45 [43].

Vortex structures and flow patterns are shown in Fig. 8 at different times. The first and dominant vortex is shed from the upstream cavity inlet and evolves from the recirculation bubble at the cavity inlet, as shown in Fig. 8a. This vortex grows rapidly within the cavity while connected to the cavity's leading edge. Growth ceases when the vortex leaves the leading edge, and the freestream is injected into the cavity and upstream of the vortex (Fig. 8b). As the primary clockwise-rotating vortex hits the trailing edge, a new counterclockwise-rotating vortex is shed into the cavity at the trailing edge (Fig. 8c), producing a high-amplitude acoustic wave. The new counterclockwise-rotating vortex then moves downstream (Fig. 8d), cutting the primary vortex (Fig. 8e). The primary vortex dictates the cavity flow's fundamental frequency and plays a crucial role in the sound generation of such flows [42].

In the next section, the height of the cavity trailing edge wall, as shown in Fig. 9, is optimized to reduce the sound perceived by an observer located at [x/D, y/D] = [2, 7.16].

B. Optimization

In this section, the noise at the observer point located at $x_{\text{obs}}/D = [2, 7.16]$ is minimized by changing the height of the cavity trailing edge wall, h_{TE} , using the MADS technique. Thus,

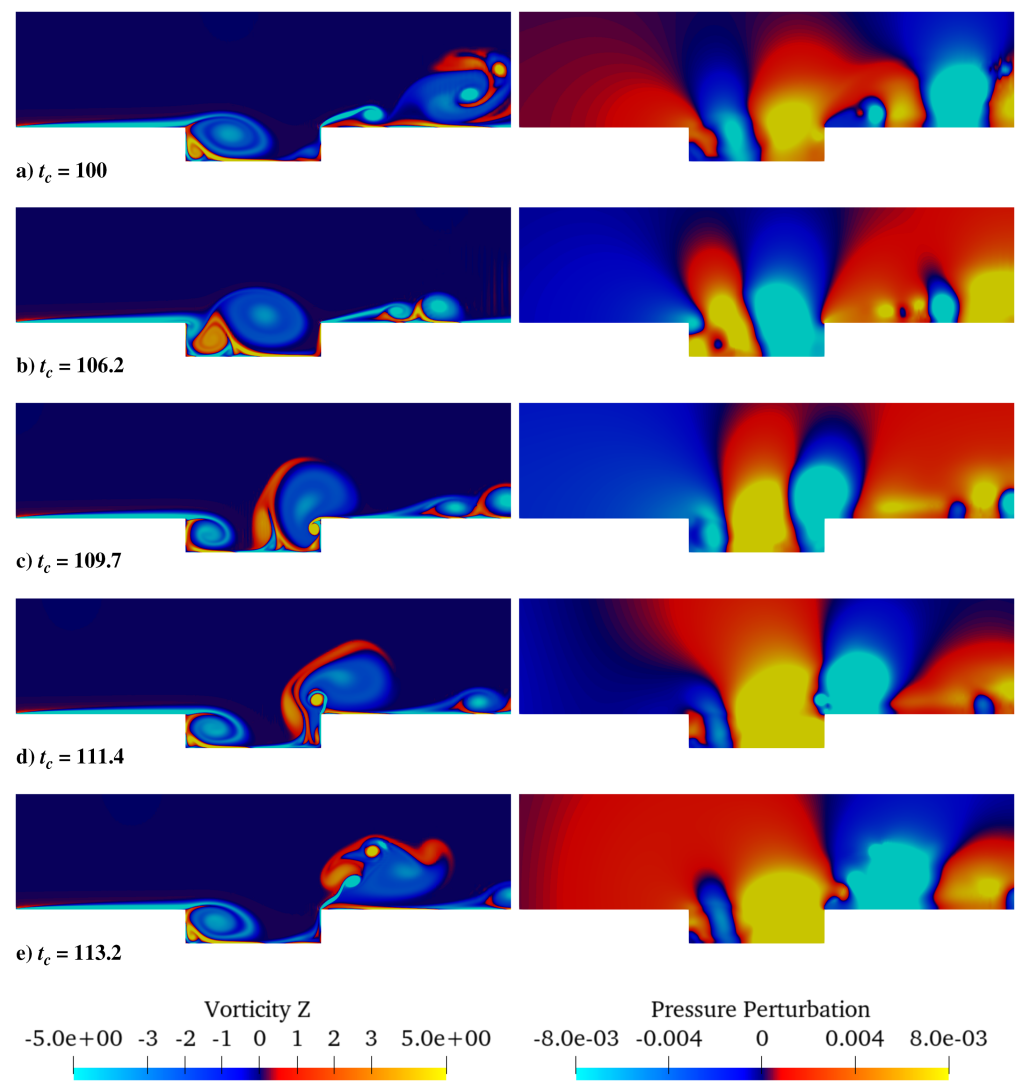


Fig. 8 The z component of the vorticity and pressure perturbation snapshots of the open cavity.

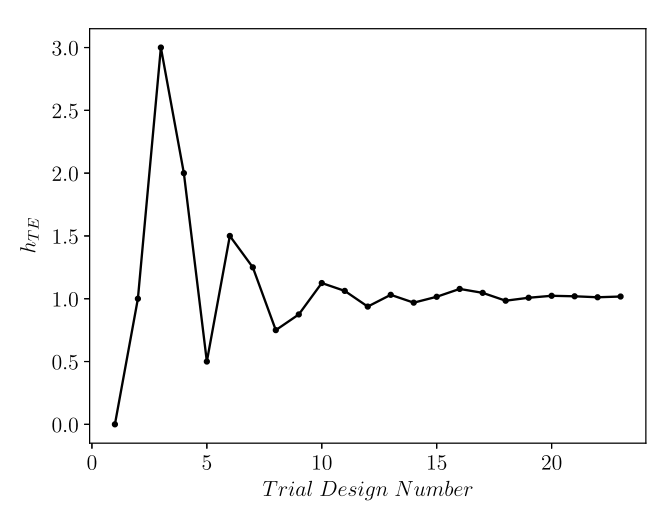


Fig. 9 The height of the two-dimensional cavity's trailing edge, used as a design variable.

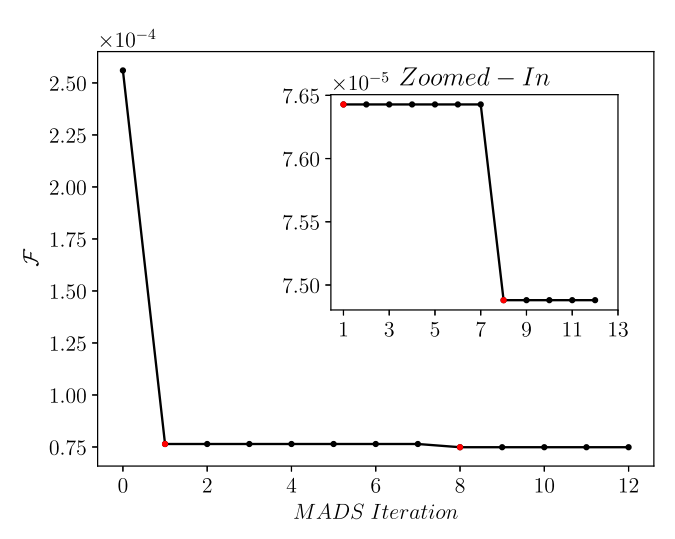
 $\mathcal{X} = [h_{TE}]$ is the design variable and $\mathcal{X}_0 = 0$, while the objective function is the root mean square of the pressure perturbation, $\mathcal{F} = p'_{rms}$.

1. Results and Discussion

Upper and lower bounds of 0 and 4, respectively, are chosen for the design variable, h_{TE} , with the objective function being the root-mean-squared of the pressure perturbation at $x_{\rm obs}$. The design variable converged to $h_{TE}=1.0156$ after 12 MADS iterations with a total of 23 objective function evaluations. The design space and the objective function convergence are shown in Fig. 10. It can be seen



a) The design space



b) The objective function convergence with the new incumbent designs highlighted in red

Fig. 10 The design space and objective function convergence for the open deep cavity.

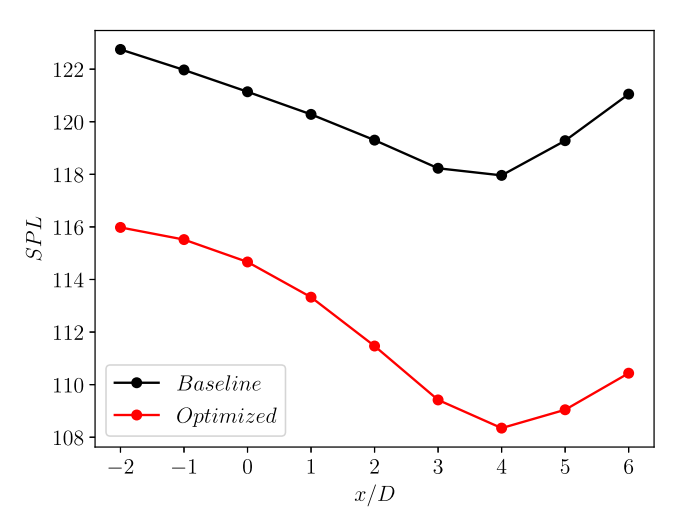


Fig. 11 The OASPL at different observer points for the optimum design of the open deep cavity.

from Fig. 10a that a wide design space is investigated by the MADS optimization technique, and only two incumbent values are found, as shown in Fig. 10b. The OASPL is decreased to 111.43 dB for the optimum design, down from 119.3 dB of the baseline design. Thus, 7.87 dB decrease in the OASPL at the observer is achieved. It can be seen from Fig. 11 that the sound at all other observer points is also reduced, as expected. The *z* component of the vorticity and pressure perturbation are plotted in Fig. 12 at different times. For the optimized shape of the open cavity, the primary clockwise vortex trapped inside the cavity reduces the emitted noise. However, there are vortices shedding off the trailing edge of the cavity, but their acoustic waves are much smaller in amplitude compared to those of the baseline design.

IV. Tandem Cylinders

The flow around two tandem cylinders consists of multiple flow features, including flow separation, reattachment, recirculation, and quasi-periodic vortex shedding, amongst others. The physics of such flows is highly dependent on the diameter ratio of the cylinders, the spacing between them, and the Reynolds number. The diameter ratio of the cylinders is defined as $r = D_d/D_u$, where D_d and D_u are the downstream and upstream diameters of the cylinders, respectively. The spacing of the cylinders, s, is defined as the distance between the rear of the upstream cylinder and the front of the downstream cylinder. These definitions are depicted in Fig. 13.

There is growing literature on flow over tandem cylinders $[\underline{45}$ — $\underline{47}]$ and the resulting acoustic field $[\underline{48}$ — $\underline{50}]$. In the next section, the flow features of two cylinders in a tandem configuration are investigated, along with the sound radiated by them, and compared with reference data $[\underline{46}]$. Finally, the diameter ratio between the cylinders and their distance are optimized to reduce the noise at the observer located 2D above the upstream cylinder.

A. Validation

In this section, the simulation of flow over tandem cylinders is validated by comparing the time history of lift and drag coefficients with the reference data [46]. The relationship between the mean time-averaged drag coefficient of the cylinders and the space between them is investigated and compared to the available literature [51].

1. Computational Details

The tandem cylinder configuration is first run for r = 1 and s = 4.5. A total of 8718 triangular and quadrilateral elements are used, and the computational grid is shown in Fig. 14. The simulation

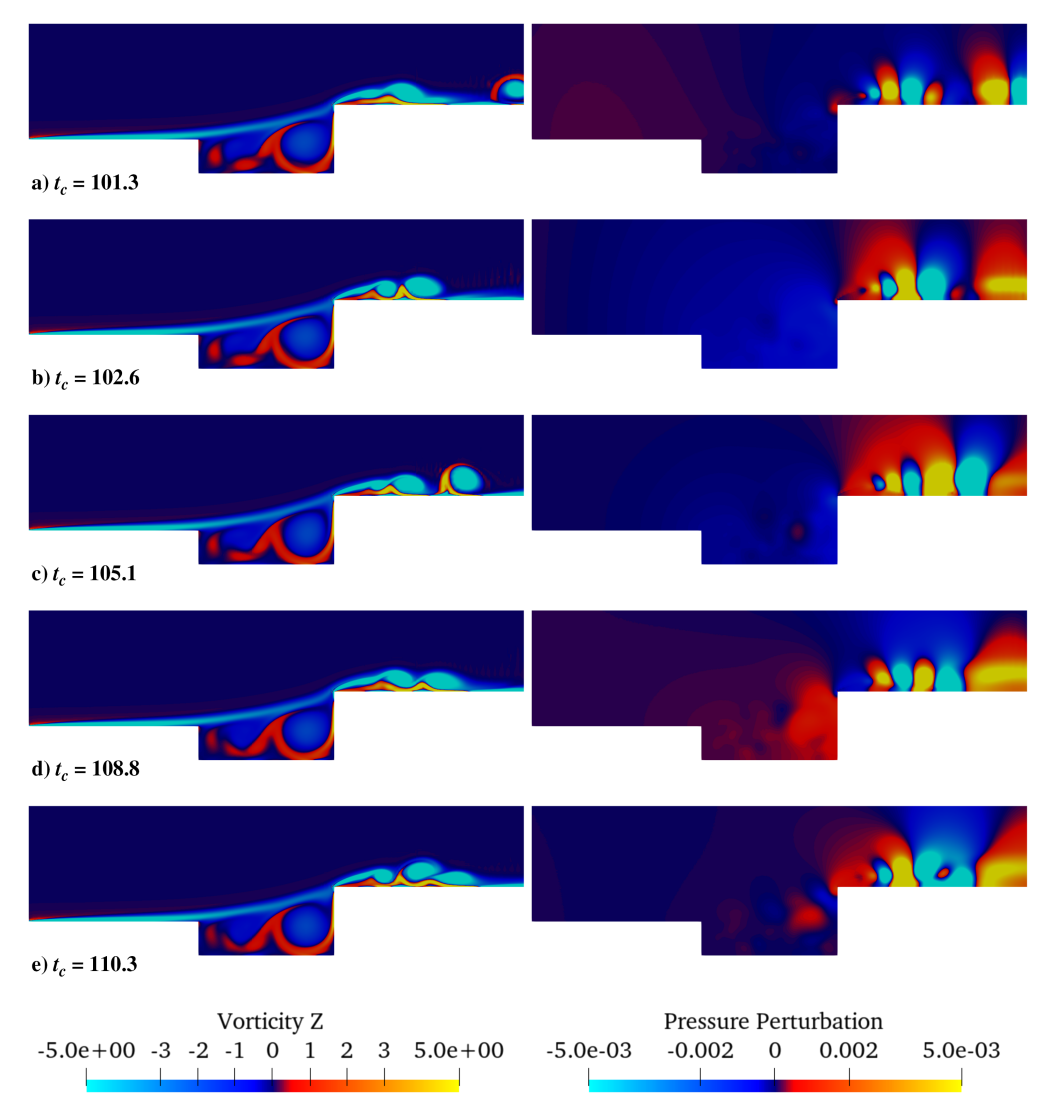
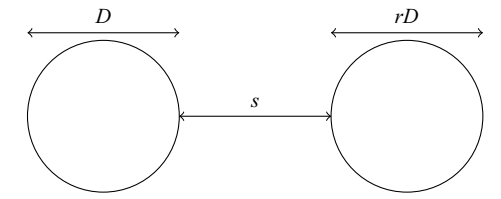


Fig. 12 The z component of the vorticity and pressure perturbation snapshots of the optimized open cavity.



 $Fig.\ 13\quad The\ arrangement\ of\ the\ tandem\ cylinders.$

is started with a $\mathcal{P}1$ simulation, switched to $\mathcal{P}2$ after $1500t_c$, and then is run for $500t_c$ to compute the statistical characteristics of the flow; $t_c = D/U_\infty$ is the time needed for flow to pass the upstream cylinder or the convective time, and U_∞ is the freestream velocity. The Reynolds number for this study is Re=200, and the inflow Mach number is $M_\infty=0.2$. The six-stage, fifth-order-accurate Explicit Singly Diagonally Implicit Runge–Kutta (ESDIRK) temporal scheme [10] is used to advance the simulation in time.

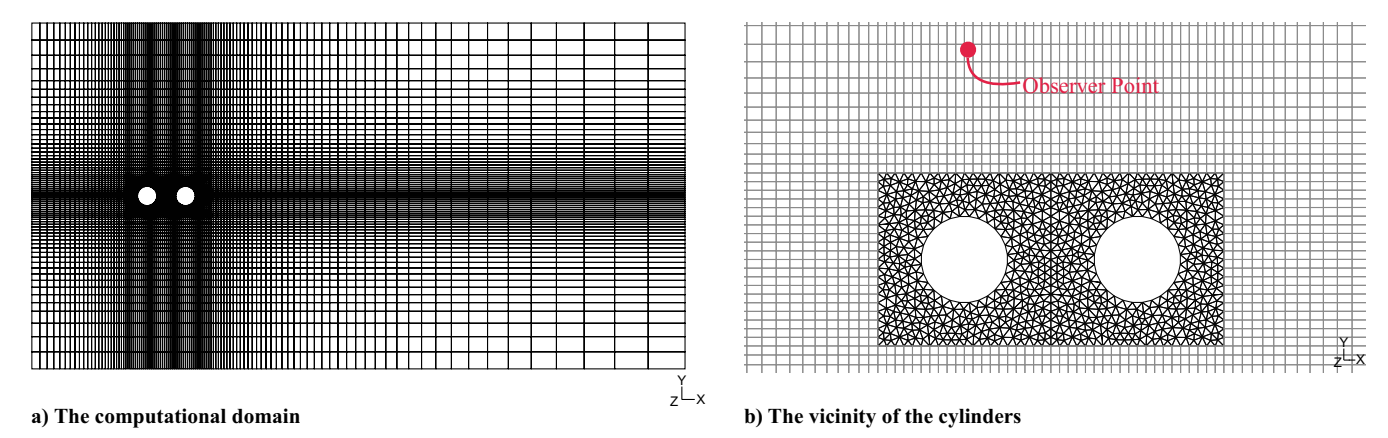
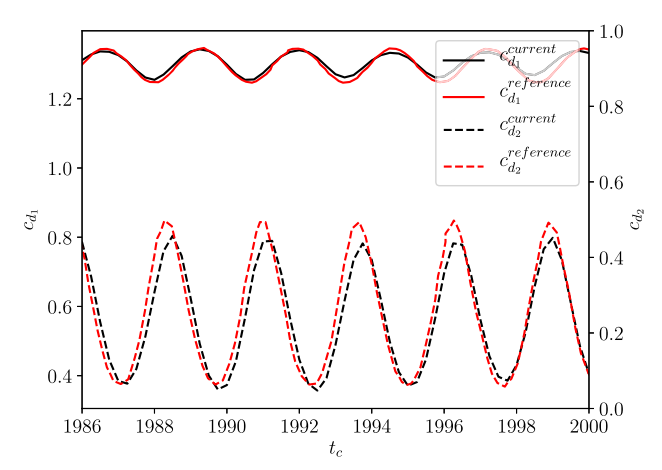


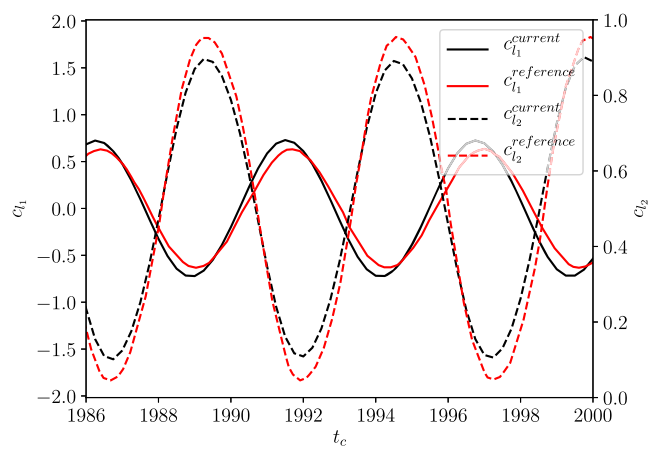
Fig. 14 The computational grid for tandem cylinders.

2. Results and Discussion

The lift and drag coefficients for both the upstream and downstream cylinders are obtained for s=4.5 and are shown in Fig. 15, where good agreement is observed comparing with reference data [46]. The drag coefficients of the two cylinders are obtained by integrating the pressure and shear stress distributions on the surface and then are averaged for 500 convective times. The time-averaged drag coefficient $\overline{c_d}$ is plotted for different values of s in Fig. 16, and it shows a similar trend to Igarashi [51]. The time-averaged drag coefficient of the



a) The drag coefficient



b) The lift coefficient

Fig. 15 The lift and drag coefficients of flow past a pair of tandem cylinders (s=4.5) at Re=200.

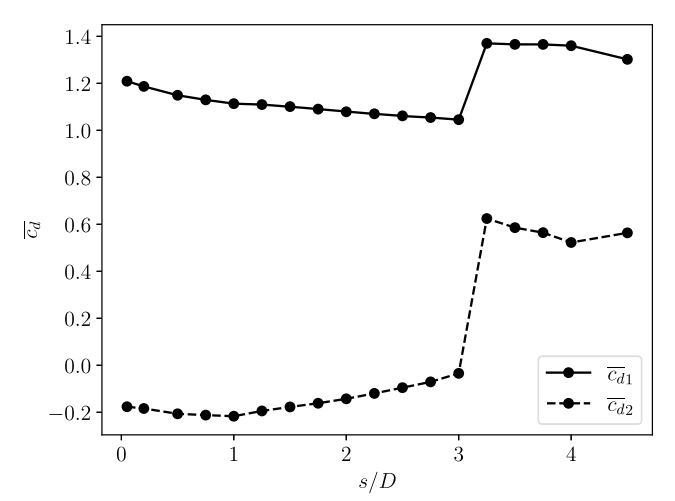


Fig. 16 Drag coefficient for the tandem cylinders versus separation ratio.

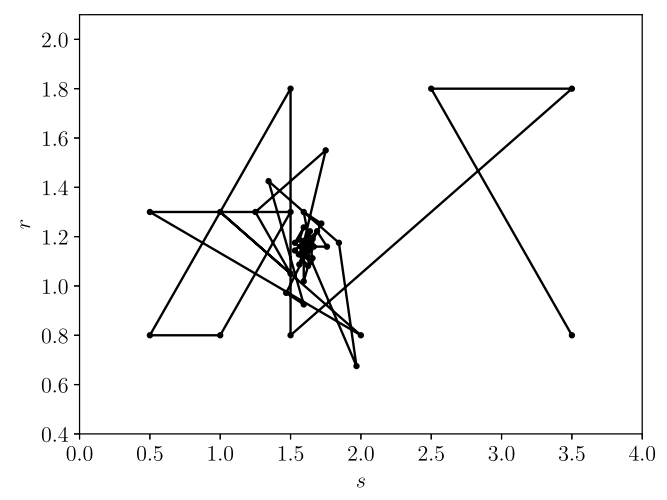
upstream cylinder, $\overline{c_{d1}}$, decreases gradually by increasing the cylinder spacing s and increases stepwise for s/D > 3. On the other hand, the time-averaged drag coefficient of the downstream cylinder, $\overline{c_{d2}}$, is negative for s/D < 3 acting as a thrust force; $\overline{c_{d2}}$ increases as the downstream cylinder is placed further away from the upstream cylinder, and a sudden increase occurs for s/D > 3.

B. Optimization

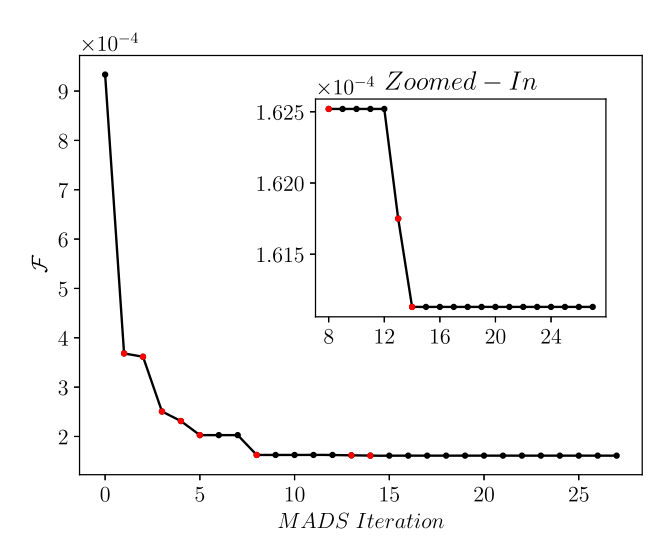
In this study, the distance between the two cylinders, s, and the ratio between the diameters of the cylinders, r, are the design variables, $\mathcal{X} = [s/D, r]$. The objective function is $\mathcal{F} = p'_{rms}$ at 2D above the upstream cylinder, depicted in Fig. 14b. Considering that the main objective of this study is to demonstrate the optimization capabilities of MADS, a loud initial design has been selected to evaluate the feasibility of optimizing toward a quieter configuration.

1. Results and Discussion

The optimization problem converges after 27 MADS iterations, including 70 objective function evaluations. The design space and objective function convergence are shown in Fig. 17, where the optimum design is found as (s/D, r) = (1.6301, 1.1594). The optimization procedure has covered a wide range of design variables, as shown in Fig. 17a. Instantaneous vorticity contours and acoustic fields are shown for the initial design and the optimum design, in Fig. 18, at $t_c = 2000$. The OASPL of the initial design at the

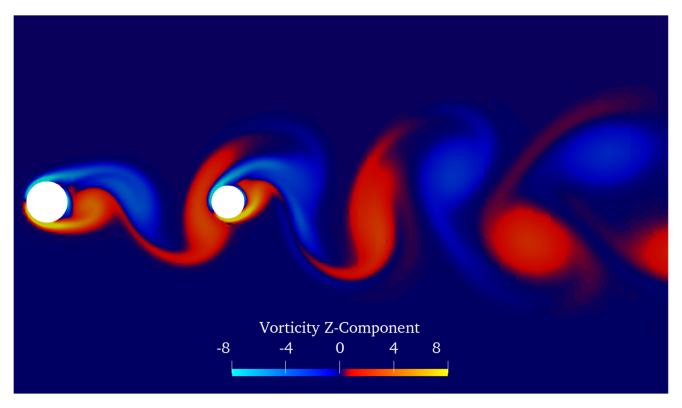


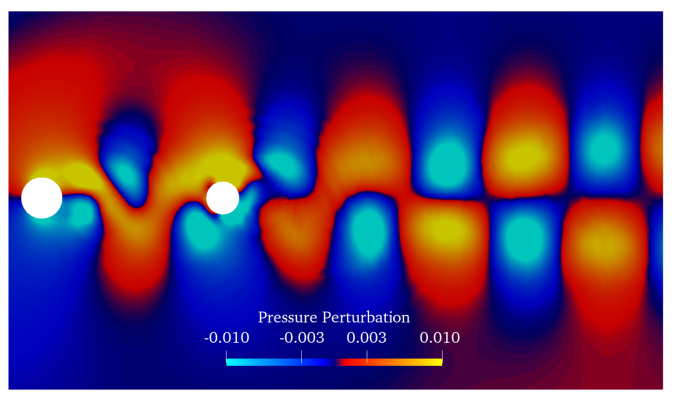
a) The design space



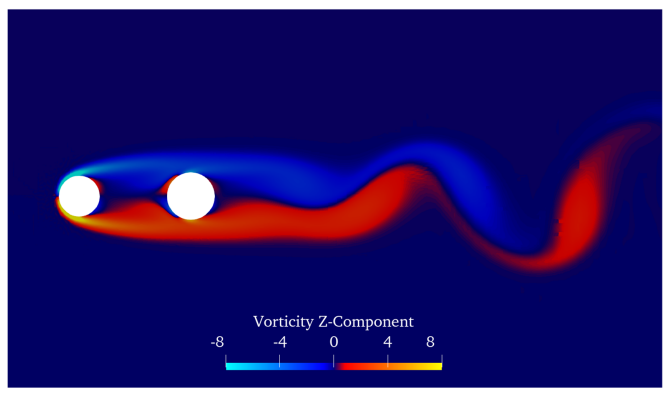
b) The objective function convergence with the new incumbent designs highlighted in red

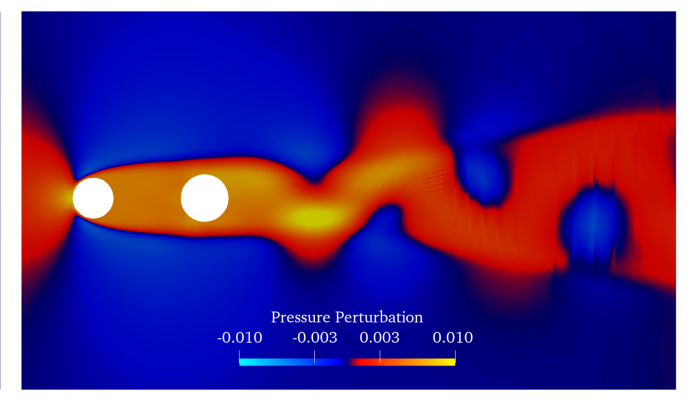
Fig. 17 The design space and objective function convergence for the tandem cylinders.





a) The initial tandem cylinder design





b) The optimum tandem cylinder design

Fig. 18 The z component of the vorticity and pressure perturbation snapshots at $t_c = 2000$.

observer, 2D above the upstream cylinder, is 136.3 dB, which reduces to 119.8 dB for the optimized configuration. Thus, a 16.5 dB decrease in overall SPL is achieved.

V. NACA0012 Airfoil

The aerodynamic characteristics of the NACA0012 airfoil have been extensively studied through experiments [52-55] and CFD simulations [56,57]. This airfoil has a relatively high maximum lift coefficient, which makes it suitable for use in low-speed applications such as general aviation, unmanned aerial vehicles (UAVs), and micro aerial vehicles (MAVs). At low Reynolds numbers, less than $Re = 10^5$, the boundary layer is laminar. In general, two different types of acoustic spectra are observed in flow past a laminar airfoil, depending on the Reynolds number and angle of attack: first, a typical tone noise phenomenon, i.e., a broadband contribution with a dominant frequency along with equidistant frequency tones, and, second, a simple broadband spectrum [58]. In the first type, the sequence of regularly spaced discrete frequency tones is due to the emergence of a separation bubble on the pressure surface close to the trailing edge [58]. On the pressure side, the hydrodynamic fluctuations are coherent in the spanwise direction [52]. Thus, it can be assumed that the governing mechanism of tonal noise is essentially two-dimensional [58].

The study of airfoil noise dates back to the 1970s, when several experimental studies showed that discrete tones are emitted from isolated airfoils [59,60], and other studies focused on understanding this phenomenon [52,54,61]. The shape of the airfoil is optimized for noise reduction in high-lift devices [62], laminar flow trailing edge [63,64], and turbulent flow trailing edge [25,65]. This study examines the laminar flow trailing edge and the aero-acoustic shape optimization of the NACA0012 airfoil at a low Reynolds number, Re = 10,000, which is the operating regime for MAVs.

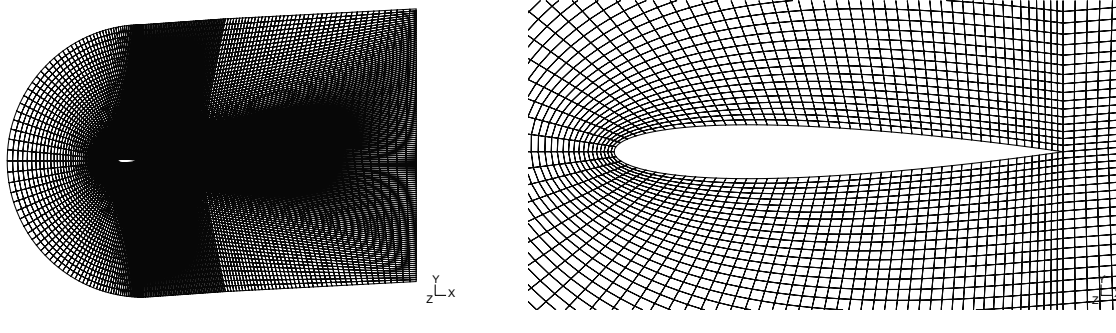
A. Validation

In this section, flow over a two-dimensional NACA0012 airfoil is validated. A grid-resolution-independence study is performed for the time-averaged lift and drag coefficients and the OASPL at an observer located a unit chord length below the trailing edge. The time-averaged lift coefficient is compared with reference direct numerical simulation (DNS) data [66] to validate the simulation.

1. Computational Details

The computational grid consists of 19,596 quadrangular elements, as depicted in Fig. 19. The domain is extended to 5c in the y direction and to 10c in the x direction, where c=1 is the chord length of the airfoil. The stretching ratio is kept below 5% everywhere in the domain. The elements in the wake region are inclined at the angle of attack to capture the vortices behind the trailing edge. The computational domain is shown in Fig. 19. The Reynolds number for this study is Re=10,000, the inflow Mach number is $M_{\infty}=0.2$, the angle of attack is 3 deg, and the Prandtl number is Pr=0.71. The simulation is run for 60 convective times, and flow statistics are averaged for the last 20 convective times. The second-order paired explicit Runge–Kutta (P-ERK) temporal scheme [67,68] is used to advance the solution in time.

Vortices leaving the computational domain can generate nonphysical acoustic wave reflections off the boundaries, contaminating the solution. Thus, the strength of such vortices must be decreased to eliminate the acoustic wave reflections off the boundaries. The addition of artificial diffusion and variable solution polynomial degrees are used in this study, as shown in Fig. 20. Artificial diffusion is applied beyond a circle with a radius of 2c centered at the trailing edge. Its magnitude increases to a maximum of 0.01 and a radius of 8c using a sinusoidal function. The solution polynomial distribution is shown in Fig. 20b, where in the vicinity of the airfoil $\mathcal{P}=3$ and it decreases to zero close to the boundaries.



a) The computational domain

b) The vicinity of the airfoil

Fig. 19 The computational grid for NACA0012 airfoil at $\alpha = 3^{\circ}$.

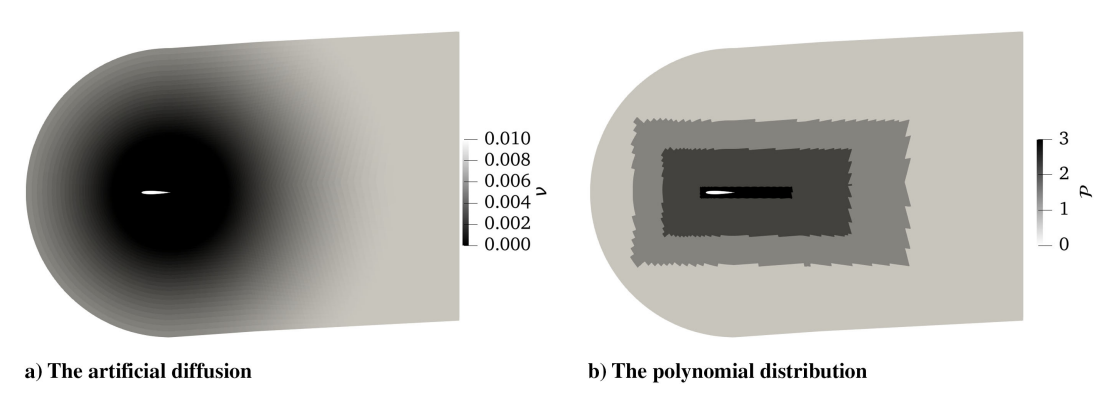


Fig. 20 The boundary treatments.

2. Results and Discussion

A different set of variable polynomial degrees is used to study the independence of the results to the grid resolution. Three different mesh resolutions are used with a maximum polynomial degree of $\mathcal{P}2$, $\mathcal{P}3$, and $\mathcal{P}4$, as shown in Fig. 21.

The time-averaged lift and drag coefficients are computed along with the OASPL at the observer located a unit chord length below the trailing edge and compared using three different grid resolutions, shown in Table $\underline{1}$. The time-averaged lift coefficient differs by less than 0.4% when the highest polynomial degree in the domain is $\mathcal{P}4$

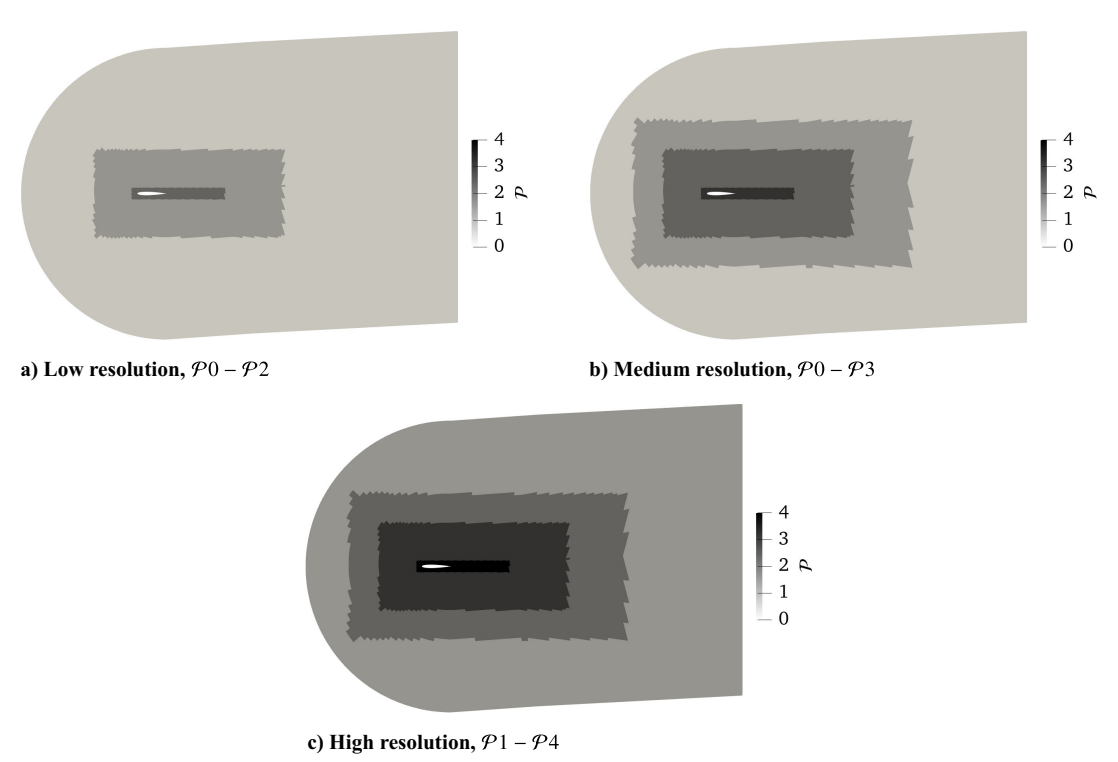


Fig. 21 The three different resolutions to study the grid resolution independency of the results.

Table 1 Averaged lift and drag coefficients and the OASPL measured at a unit chord distance below the trailing edge of the baseline NACA0012

Parameter	P0 - P2	P0 - P3	P1 - P4
$\overline{c_l}$	0.0877	0.0886	0.0889
$\overline{c_d}$	0.0448	0.0447	0.0447
OASPL, dB	109.59	110.00	110.53

compared to that of $\mathcal{P}3$, while the time-averaged drag coefficient remains the same by three significant digits. The time-averaged lift coefficient obtained via the $\mathcal{P}0-\mathcal{P}3$ simulation agrees well with the DNS data [66]. Furthermore, the OASPL difference between $\mathcal{P}0-\mathcal{P}3$ and $\mathcal{P}1-\mathcal{P}4$ simulations is 0.53 dB or 0.48%. Thus, it is concluded that the grid resolution for $\mathcal{P}0-\mathcal{P}3$ simulation is sufficient for this problem.

The sensitivity of the time-averaged quantities to the averaging window is investigated by choosing two different averaging windows. The lift and drag coefficients are averaged over 20 and 40 convective time windows, as shown in Table 2. The difference between the time-averaged lift and drag coefficients for both averaging window lengths is negligible. Thus, the quantities are averaged over 20 convective time windows.

The time history of lift and drag coefficients is shown in Fig. $\underline{22}$ for the last two convective times. The periodic behavior of c_l and c_d is associated with the periodic vortex shedding at the trailing edge.

The pressure perturbation at $t_c=60$ is shown in Fig. <u>25a</u>. Acoustic waves are generated close to the trailing edge and propagate everywhere in the domain. There are no visible acoustic wave reflections off the boundaries, showing the effectiveness of the boundary treatments used in this study. The amplitude of the pressure perturbations is higher in the wake region and behind the trailing edge, where the vortices are shed and travel downstream. The addition of artificial viscosity, as shown in Fig. <u>20a</u>, dampens these vortices and consequently reduces the amplitude of acoustic waves far from the trailing edge.

Table 2 Averaging window sensitivity of the timeaveraged quantities

Parameter	$20t_c$	40t _c
\bar{c}_l	0.08857	0.08863
$ar{c_d}$	0.04472	0.04473

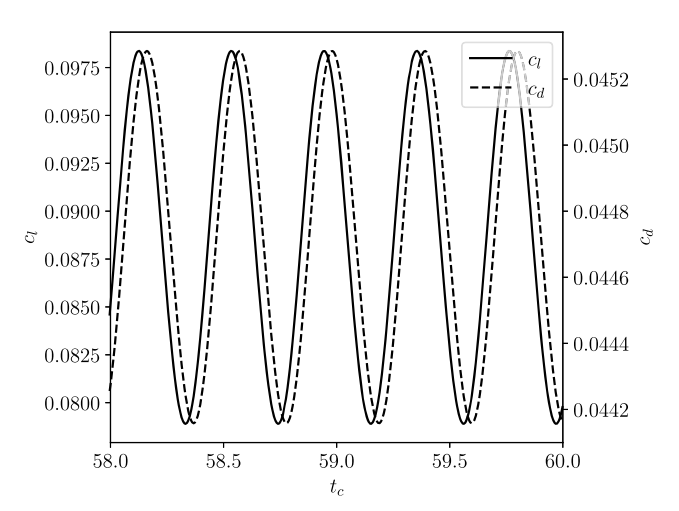


Fig. 22 Time-histories of lift and drag coefficients.

B. Optimization

In this section, the noise at an observer located at a unit chord length below the trailing edge is reduced. A total of four design parameters are chosen based on the NACA four-digit airfoil series. The maximum camber c_{\max}^a ; the distance of maximum camber from the airfoil leading edge, $x_{c_{\max}^a}$; maximum thickness of the airfoil, t_{\max}^a ; and the angle of attack α are the four design parameters, i.e., $\mathcal{X} = [c_{\max}^a, x_{c_{\max}^a}, t_{\max}^a, \alpha]$, as depicted in Fig. 23. The simulation is first run 60 convective times for each objective function evaluation. Then the time-averaged pressure is computed from $20t_c$ to $40t_c$, \bar{p}_{20-40} , and then from $40t_c$ to $60t_c$, \bar{p}_{40-60} . If the difference between \bar{p}_{20-40} and \bar{p}_{40-60} is above 1%, the simulation is run for 20 more convective times. The simulation is run long enough so that the difference between two consecutive time-averaged pressure signals, over $20t_c$, is below 1%.

1. Results and Discussion

The optimization procedure is run using a maximum polynomial degree of $\mathcal{P}3$, as shown in Fig. 21b. The maximum camber range is set to $c_{\max}^a \in [-10,10]$ as a percentage of the chord, with the distance from the airfoil leading edge in the range of $x_{c_{\max}}^a \in [2,9]$ as a tenth of the chord. The maximum thickness of the airfoil is within the range of $t_{\max}^a \in [8,16]$ as a percentage of the chord. Finally, the angle of attack varies from -5° to 5° . The objective function is defined as the OASPL at the observer, with constraints on both the mean lift and mean drag coefficients. A quadratic penalty term is added to the objective function when the lift coefficient deviates from the baseline design, and an additional quadratic penalty term is added when the mean drag coefficient is above the baseline design. The objective function is defined as

$$\mathcal{F} = \begin{cases} OASPL + \epsilon (\overline{c_l} - \overline{c_{l,\text{baseline}}})^2 + \epsilon (\overline{c_d} - \overline{c_{d,\text{baseline}}})^2 & \overline{c_d} > \overline{c_{d,\text{baseline}}} \\ OASPL + \epsilon (\overline{c_l} - \overline{c_{l,\text{baseline}}})^2 & \overline{c_d} \leq \overline{c_{d,\text{baseline}}} \end{cases}$$

$$(22)$$

where the constant ϵ is set to 400,000 to compensate for the order of magnitude difference in *OASPL* and $\overline{c_l}$ and $\overline{c_d}$. The defined objective function minimizes the OASPL while maintaining the mean lift coefficient, and it ensures that the optimized airfoil has a similar or lower mean drag coefficient.

This optimization procedure converges after 39 MADS iterations, consisting of 149 objective function evaluations. The design space and the convergence of the objective function are shown in Fig. 24. The optimal airfoil design has a maximum camber of $c_{\rm max}^a = -0.8944\%$ of the chord, at a 2.1428-tenth of the chord distance from the leading edge, with a thickness of $t_{\rm max}^a = 9.1309\%$ of the chord, at an angle of attack of $\alpha = 1.9350$ deg. The optimized airfoil is silent with OASPL = 0 dB, maintains an unchanged mean lift coefficient of $\overline{c_l} = 0.0886$, and achieves a reduced mean drag coefficient by

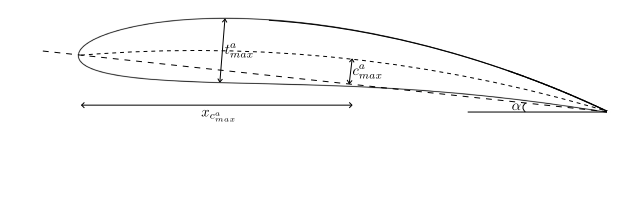




Fig. 23 The design variables and the observer point located at a unit chord length below the trailing edge for the two-dimensional NACA four-digit airfoil.

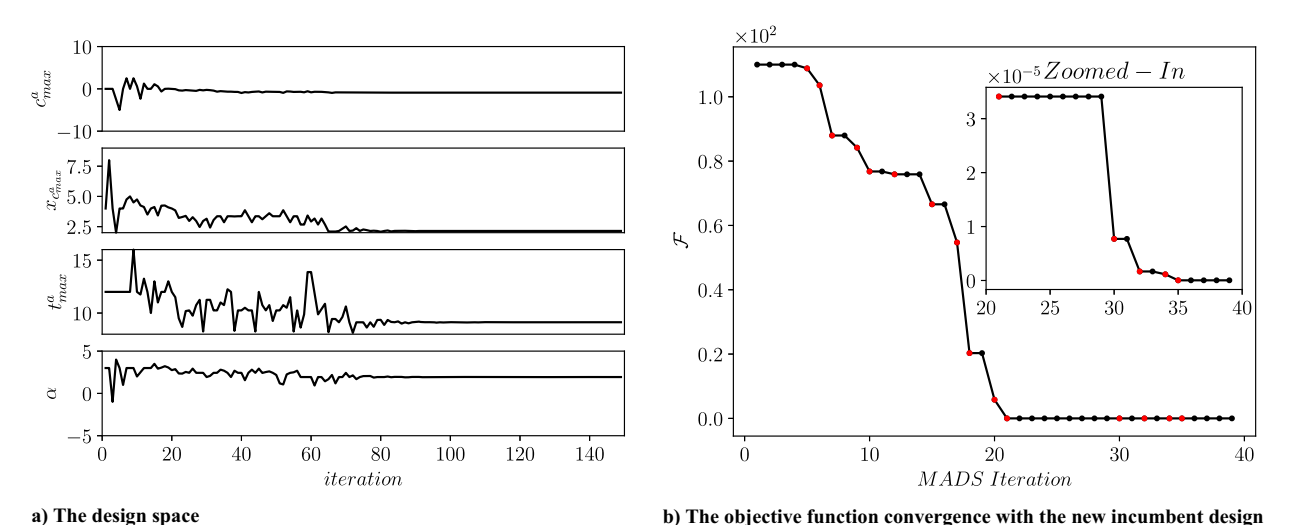


Fig. 24 The design space and objective function convergence for $\mathcal{P}3$ optimization of the NACA four-digit airfoil.

highlighted in red

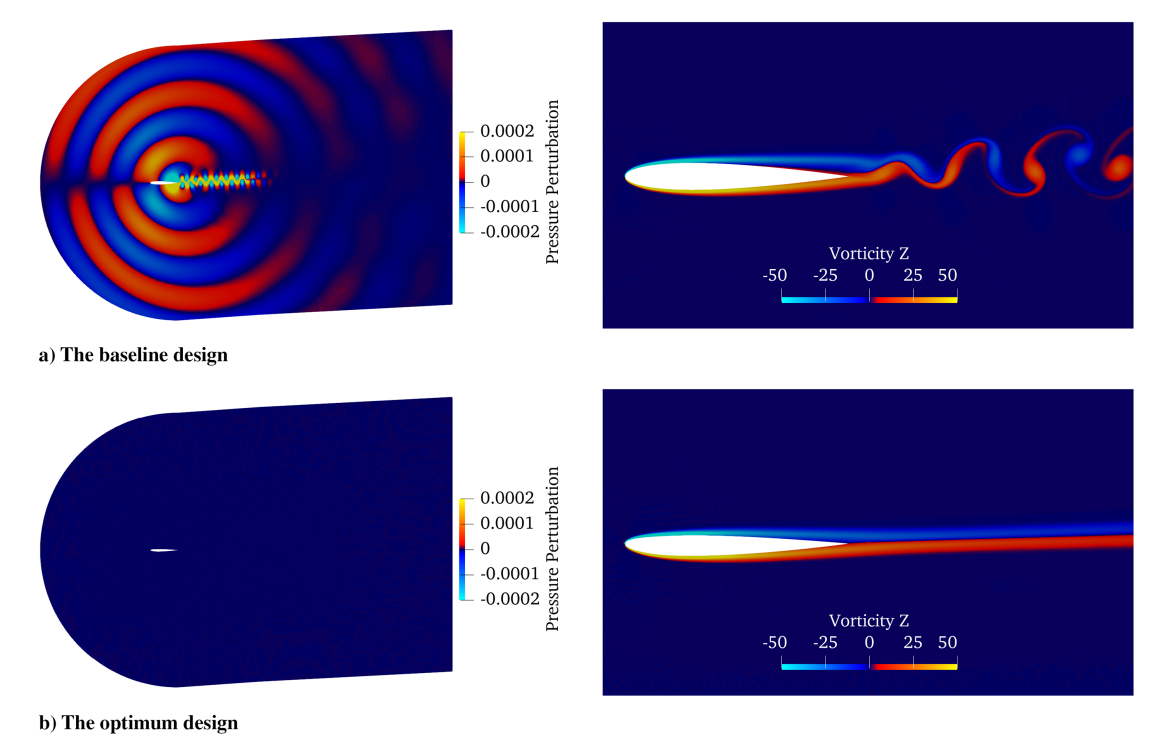


Fig. 25 The pressure perturbation and vorticity in the z direction for the baseline and $\mathcal{P}3$ optimization designs of NACA four-digit airfoil at $t_c = 60$.

24.95% to $\overline{c_d} = 0.0348$. And, finally, the pressure perturbation and z component of vorticity are shown in Fig. <u>25</u> for the baseline and optimum designs. In the baseline design, the flow is attached to the airfoil on the pressure side, and flow instability occurs on the suction side. A periodic vortex shedding takes place as the flow passes over the trailing edge, resulting in acoustic wave generation. However, in the optimum design, the flow instability is eliminated, resulting in a silent airfoil.

VI. Conclusions

This paper demonstrates the efficacy of using the high-order FR method, direct acoustic computation, and MADS optimization technique for aeroacoustic shape optimization. Three case studies were presented, demonstrating that significant noise reduction could be achieved by optimizing the geometry of two-dimensional objects at low Reynolds numbers. These findings have practical applications in various industries, including aerospace, automotive, and wind

turbine design, where noise reduction is crucial. We note that the simulations undertaken here are relatively inexpensive twodimensional problems. The computational cost of performing three-dimensional scale-resolving simulations, such as large eddy simulation (LES) or DNS, is significantly higher than those in previous aerodynamic optimization studies due to domain size and resolution requirements [15,69]. Additionally, we propose that adaptivity and novel time-stepping algorithms are two possible methods for reducing the computational cost of future LES or DNS simulations [68,70,71]. Despite this, the current work demonstrates the feasibility of the approach and lays a foundation for future LES or DNS aeroacoustic optimization studies, provided appropriate computational resources. Future research could extend this approach to more complex geometries, higher dimensions, and higher Reynolds numbers to explore the potential limits of the optimization technique and broaden its applications. While the baseline designs were validated against reference numerical simulations, there are currently no reference datasets for the newly optimized designs. In future studies,

it would be prudent to conduct experimental studies using anechoic wind tunnels in the optimized configurations to validate the numerical results presented herein.

Data Statement

Data relating to the results in this paper can be downloaded from the publication's website under a CC-BY-NC-ND 4.0 license.

Acknowledgments

The authors acknowledge support from the Natural Sciences and Engineering Research Council of Canada (NSERC; RGPIN-2017-06773) and the Fonds de recherche du Québec (FRQNT) via the Nouveaux chercheurs program.

References

- [1] Burden of Disease from Environmental Noise: Quantification of Healthy Life Years Lost in Europe, World Health Organization Regional Office for Europe, 2011.
- [2] Mahashabde, A., Wolfe, P., Ashok, A., Dorbian, C., He, Q., Fan, A., Lukachko, S., Mozdzanowska, A., Wollersheim, C., Barrett, S., et al., "Assessing the Environmental Impacts of Aircraft Noise and Emissions," *Progress in Aerospace Sciences*, Vol. 47, No. 1, 2011, pp. 15–52. https://doi.org/10.1016/j.paerosci.2010.04.003
- [3] Basner, M., Clark, C., Hansell, A., Hileman, J., Janssen, S., Shepherd, K., and Sparrow, V., "Aviation Noise Impacts: State of the Science," *Noise & Health*, Vol. 19, No. 87, 2017, p. 41.
- [4] Pepper, C., Nascarella, M., and Kendall, R., "A Review of the Effects of Aircraft Noise on Wildlife and Humans, Current Control Mechanisms, and the Need for Further Study," *Environmental Management*, Vol. 32, Oct. 2003, pp. 418–432. https://doi.org/10.1007/s00267-003-3024-4
- [5] "Global Outlook for Air Transport," International Air Transport Association (IATA) TR, June 2022, https://www.iata.org/en/iata-repository/publications/economic-reports/airline-industry-economic-performance---june-2022---report/.
- [6] Tam, C., "Recent Advances in Computational Aeroacoustics," Fluid Dynamics Research, Vol. 38, No. 9, 2006, p. 591. https://doi.org/10.1016/j.fluiddyn.2006.03.006
- [7] Huynh, H., "A Flux Reconstruction Approach to High-Order Schemes Including Discontinuous Galerkin Methods," 18th AIAA Computational Fluid Dynamics Conference, AIAA Paper 2007-4079, 2007. https://doi.org/10.2514/6.2007-4079
- [8] Moura, R., Sherwin, S., and Peiró, J., "Linear Dispersion-Diffusion Analysis and Its Application to Under-Resolved Turbulence Simulations Using Discontinuous Galerkin Spectral/hp Methods," *Journal of Computational Physics*, Vol. 298, Oct. 2015, pp. 695–710. https://doi.org/10.1016/j.jcp.2015.06.020
- [9] Vincent, P., Castonguay, P., and Jameson, A., "Insights from von Neumann Analysis of High-Order Flux Reconstruction Schemes," *Journal of Computational Physics*, Vol. 230, No. 22, 2011, pp. 8134–8154. https://doi.org/10.1016/j.jcp.2011.07.013
- [10] Vermeire, B., and Vincent, P., "On the Behaviour of Fully-Discrete Flux Reconstruction Schemes," *Computer Methods in Applied Mechanics and Engineering*, Vol. 315, March 2017, pp. 1053–1079. https://doi.org/10.1016/j.cma.2016.11.019
- [11] Vincent, P., Witherden, F., Vermeire, B., Park, J., and Iyer, A., "Towards Green Aviation with Python at Petascale," SC'16: Proceedings of the International Conference for High Performance Computing, Networking, Storage and Analysis, Inst. of Electrical and Electronics Engineers, New York, 2016, pp. 1–11. https://doi.org/10.1109/SC.2016.1
- [12] Johnson, C., "On Computatibility and Error Control in CFD," International Journal for Numerical Methods in Fluids, Vol. 20, Nos. 8–9, 1995, pp. 777–788. https://doi.org/10.1002/fld.1650200806
- [13] Chen, G., and Fidkowski, K., "Discretization Error Control for Constrained Aerodynamic Shape Optimization," *Journal of Computational Physics*, Vol. 387, June 2019, pp. 163–185. https://doi.org/10.1016/j.jcp.2019.02.038
- [14] Martins, J., and Lambe, A., "Multidisciplinary Design Optimization: A Survey of Architectures," AIAA Journal, Vol. 51, No. 9, 2013, pp. 2049–2075. https://doi.org/10.2514/1.J051895
- [15] Karbasian, H., and Vermeire, B., "Gradient-Free Aerodynamic Shape Optimization Using Large Eddy Simulation," Computers & Fluids,

- Vol. 232, Jan. 2022, Paper 105185. https://doi.org/10.1016/j.compfluid.2021.105185
- [16] Forrest, S., "Genetic Algorithms," ACM Computing Surveys (CSUR), Vol. 28, No. 1, 1996, pp. 77–80.
- [17] Schmitt, L., "Theory of Genetic Algorithms II: Models for Genetic Operators over the String-Tensor Representation of Populations and Convergence to Global Optima for Arbitrary Fitness Function Under Scaling," *Theoretical Computer Science*, Vol. 310, Nos. 1–3, 2004, pp. 181–231.
 - https://doi.org/10.1016/S0304-3975(03)00393-1
- [18] Praveen, C., and Duvigneau, R., "Low Cost PSO Using Metamodels and Inexact Pre-Evaluation: Application to Aerodynamic Shape Design," Computer Methods in Applied Mechanics and Engineering, Vol. 198, Nos. 9–12, 2009, pp. 1087–1096. https://doi.org/10.1016/j.cma.2008.11.019
- [19] Wang, Y., Zhang, B., and Chen, Y., "Robust Airfoil Optimization Based on Improved Particle Swarm Optimization Method," *Applied Mathematics and Mechanics*, Vol. 32, 2011, pp. 1245–1254. https://doi.org/10.1007/s10483-011-1497-x
- [20] Zhang, Y., Wang, S., Ji, G., et al., "A Comprehensive Survey on Particle Swarm Optimization Algorithm and Its Applications," *Mathematical Problems in Engineering*, Vol. 2015, Feb. 2015. https://doi.org/10.1155/2015/931256
- [21] Audet, C., and Dennis, J., Jr., "Mesh Adaptive Direct Search Algorithms for Constrained Optimization," SIAM Journal on Optimization, Vol. 17, No. 1, 2006, pp. 188–217. https://doi.org/10.1137/040603371
- [22] Luo, J., Xiong, J., and Liu, F., "Aerodynamic Design Optimization by Using a Continuous Adjoint Method," SCIENCE CHINA Physics, Mechanics & Astronomy, Vol. 57, 2014, pp. 1363–1375. https://doi.org/10.1007/s11433-014-5479-0
- [23] Lyu, Z., Kenway, G., and Martins, J., "Aerodynamic Shape Optimization Investigations of the Common Research Model Wing Benchmark," AIAA Journal, Vol. 53, No. 4, 2015, pp. 968–985. https://doi.org/10.2514/1.J053318
- [24] Aubry, A., Karbasian, H., and Vermeire, B., "High-Fidelity Gradient-Free Optimization of Low-Pressure Turbine Cascades," *Computers & Fluids*, Vol. 248, Nov. 2022, Paper 105668. https://doi.org/10.1016/j.compfluid.2022.105668
- [25] Marsden, A., Wang, M., Dennis, J., and Moin, P., "Trailing-Edge Noise Reduction Using Derivative-Free Optimization and Large-Eddy Simulation," *Journal of Fluid Mechanics*, Vol. 572, Feb. 2007, pp. 13–36. https://doi.org/10.1017/S0022112006003235
- [26] Kholodov, P., and Moreau, S., "Optimization of Serrations for Broad-band Trailing-Edge Noise Reduction Using an Analytical Model," 25th AIAA/CEAS Aeroacoustics Conference, AIAA Paper 2019-2655, 2019. https://doi.org/10.2514/6.2019-2655
- [27] Rottmayer, J., Özkaya, E., Satcunanathan, S., Zhou, B., Aehle, M., Gauger, N., Meinke, M., Schröder, W., and Pullin, S., "Trailing-Edge Noise Reduction Using Porous Treatment and Surrogate-Based Global Optimization," arXiv preprint arXiv:2301.13047, 2023. https://doi.org/10.48550/arXiv.2301.13047
- [28] Xue, D., Yan, Q., Li, Z., and Wei, K., "Multidisciplinary Optimization Design of Low-Noise Propellers," *Aerospace*, Vol. 10, No. 3, 2023, p. 254. https://doi.org/10.3390/aerospace10030254
- [29] Peixun, Y., Jiahui, P., Junqiang, B., Xiao, H., and Xiang, S., "Aeroa-coustic and Aerodynamic Optimization of Propeller Blades," *Chinese Journal of Aeronautics*, Vol. 33, No. 3, 2020, pp. 826–839. https://doi.org/10.1016/j.cja.2019.11.005
- [30] Marinus, B., Roger, M., and Van Den Braembussche, R., "Aeroacoustic and Aerodynamic Optimization of Aircraft Propeller Blades," 16th AIAA/CEAS Aeroacoustics Conference, AIAA Paper 2010-3850, 2010. https://doi.org/10.2514/6.2010-3850
- [31] Vermeire, B., Witherden, F., and Vincent, P., "On the Utility of GPU Accelerated High-Order Methods for Unsteady Flow Simulations: A Comparison with Industry-Standard Tools," *Journal of Computational Physics*, Vol. 334, April 2017, pp. 497–521. https://doi.org/10.1016/j.jcp.2016.12.049
- [32] Vermeire, B. C., Nadarajah, S., and Tucker, P. G., "Implicit Large Eddy Simulation Using the High-Order Correction Procedure via Reconstruction Scheme," *International Journal for Numerical Methods in Fluids*, Vol. 82, No. 5, 2016, pp. 231–260. https://doi.org/10.1002/fld.4214
- [33] Hamedi, M., and Vermeire, B., "Optimized Filters for Stabilizing High-Order Large Eddy Simulation," *Computers & Fluids*, Vol. 237, April 2022, Paper 105301. https://doi.org/10.1016/j.compfluid.2021.105301

- [34] Wang, Z., and Gao, H., "A Unifying Lifting Collocation Penalty Formulation Including the Discontinuous Galerkin, Spectral Volume/ Difference Methods for Conservation Laws on Mixed Grids," *Journal of Computational Physics*, Vol. 228, No. 21, 2009, pp. 8161–8186. https://doi.org/10.1016/j.jcp.2009.07.036
- [35] Williams, D., Shunn, L., and Jameson, A., "Symmetric Quadrature Rules for Simplexes Based on Sphere Close Packed Lattice Arrangements," *Journal of Computational and Applied Mathematics*, Vol. 266, Aug. 2014, pp. 18–38. https://doi.org/10.1016/j.cam.2014.01.007
- [36] Torczon, V., "On the Convergence of Pattern Search Algorithms," SIAM Journal on Optimization, Vol. 7, No. 1, 1997, pp. 1–25. https://doi.org/10.1137/S1052623493250780
- [37] Coope, I., and Price, C., "On the Convergence of Grid-Based Methods for Unconstrained Optimization," SIAM Journal on Optimization, Vol. 11, No. 4, 2001, pp. 859–869. https://doi.org/10.1137/S1052623499354989
- [38] Davis, C., "Theory of Positive Linear Dependence," American Journal of Mathematics, Vol. 76, No. 4, 1954, pp. 733–746. https://doi.org/10.2307/2372648
- [39] Gharib, M., and Roshko, A., "The Effect of Flow Oscillations on Cavity Drag," *Journal of Fluid Mechanics*, Vol. 177, April 1987, pp. 501–530. https://doi.org/10.1017/S002211208700106X
- [40] Colonius, T., Basu, A., and Rowley, C., "Numerical Investigation of the Flow Past a Cavity," 5th AIAA/CEAS Aeroacoustics Conference and Exhibit, AIAA Paper 1999-1912, 1999. https://doi.org/10.2514/6.1999-1912
- [41] Rowley, C., Colonius, T., and Basu, A., "On Self-Sustained Oscillations in Two-Dimensional Compressible Flow over Rectangular Cavities," *Journal of Fluid Mechanics*, Vol. 455, March 2002, pp. 315–346. https://doi.org/10.1017/S0022112001007534
- [42] Larsson, J., Davidson, L., Olsson, M., and Eriksson, L., "Aeroacoustic Investigation of an Open Cavity at Low Mach Number," *AIAA Journal*, Vol. 42, No. 12, 2004, pp. 2462–2473. https://doi.org/10.2514/1.1339
- [43] Ask, J., and Davidson, L., "Sound Generation and Radiation of an Open Two-Dimensional Cavity," AIAA Journal, Vol. 47, No. 6, 2009, pp. 1337–1349. https://doi.org/10.2415/1.32595
- [44] Martin, R., Soria, M., Lehmkuhl, O., Gorobets, A., and Duben, A., "Noise Radiated by an Open Cavity at Low Mach Number: Effect of the Cavity Oscillation Mode," *International Journal of Aeroacoustics*, Vol. 18, Nos. 6–7, 2019, pp. 647–668. https://doi.org/10.1177/1475472X19871534
- [45] Shan, X., "Effect of an Upstream Cylinder on the Wake Dynamics of Two Tandem Cylinders with Different Diameters at Low Reynolds Numbers," *Physics of Fluids*, Vol. 33, No. 8, 2021, Paper 083605. https://doi.org/10.1063/5.0060065
- [46] Ding, H., Shu, C., Yeo, K., and Xu, D., "Numerical Simulation of Flows Around Two Circular Cylinders by Mesh-Free Least Square-Based Finite Difference Methods," *International Journal for Numerical Methods in Fluids*, Vol. 53, No. 2, 2007, pp. 305–332. https://doi.org/10.1002/fld.1281
- [47] Sharman, B., Lien, F., Davidson, L., and Norberg, C., "Numerical Predictions of Low Reynolds Number Flows over Two Tandem Circular Cylinders," *International Journal for Numerical Methods in Fluids*, Vol. 47, No. 5, 2005, pp. 423–447. https://doi.org/10.1002/fld.812
- [48] Fitzpatrick, J., "Flow/Acoustic Interactions of Two Cylinders in Cross-Flow," *Journal of Fluids and Structures*, Vol. 17, No. 1, 2003, pp. 97–113. https://doi.org/10.1016/S0889-9746(02)00091-9
- [49] Mohany, A., and Ziada, S., "Numerical Simulation of the Flow-Sound Interaction Mechanisms of a Single and Two-Tandem Cylinders in Cross-Flow," *Journal of Pressure Vessel Technology*, Vol. 131, No. 3, 2009.
 - https://doi.org/10.1115/1.3110029
- [50] Finnegan, S., Meskell, C., and Ziada, S., "Experimental Investigation of the Acoustic Power Around Two Tandem Cylinders," *Journal of Pressure Vessel Technology*, Vol. 132, No. 4, 2010. https://doi.org/10.1115/1.4001701
- [51] Igarashi, T., "Characteristics of the Flow Around Two Circular Cylinders Arranged in Tandem: 1st Report," *Bulletin of JSME*, Vol. 24, No. 188, 1981, pp. 323–331. https://doi.org/10.1299/jsme1958.24.323
- [52] Paterson, R., Vogt, P., Fink, M., and Munch, C., "Vortex Noise of Isolated Airfoils," *Journal of Aircraft*, Vol. 10, No. 5, 1973, pp. 296–302. https://doi.org/10.2514/3.60229

- [53] Longhouse, R., "Vortex Shedding Noise of Low Tip Speed, Axial Flow Fans," *Journal of Sound and Vibration*, Vol. 53, No. 1, 1977, pp. 25–46. https://doi.org/10.1016/0022-460X(77)90092-X
- [54] Arbey, H., and Bataille, J., "Noise Generated by Airfoil Profiles Placed in a Uniform Laminar Flow," *Journal of Fluid Mechanics*, Vol. 134, Sept. 1983, pp. 33–47. https://doi.org/10.1017/S0022112083003201
- [55] Nash, E., Lowson, M., and McAlpine, A., "Boundary-Layer Instability Noise on Aerofoils," *Journal of Fluid Mechanics*, Vol. 382, March 1999, pp. 27–61. https://doi.org/10.1017/S002211209800367X
- [56] Atobe, T., and Ikeda, T., "Flow Instability Around a 2D Airfoil Induced by Acoustic Disturbances at Low Reynolds Numbers," *Proceedings of* the 27th Congress of International Council of Aeronautical Sciences, 2010, pp. 1–13.
- [57] Ikeda, T., Atobe, T., and Takagi, S., "Direct Simulations of Trailing-Edge Noise Generation from Two-Dimensional Airfoils at Low Reynolds Numbers," *Journal of Sound and Vibration*, Vol. 331, No. 3, 2012, pp. 556–574. https://doi.org/10.1016/j.jsv.2011.09.019
- [58] Desquesnes, G., Terracol, M., and Sagaut, P., "Numerical Investigation of the Tone Noise Mechanism over Laminar Airfoils," *Journal of Fluid Mechanics*, Vol. 591, Nov. 2007, pp. 155–182. https://doi.org/10.1017/S0022112007007896
- [59] Clark, L., "The Radiation of Sound from an Airfoil Immersed in a Laminar Flow," *Journal of Engineering for Gas Turbines and Power*, 1971. https://doi.org/10.1115/1.3445595
- [60] Hersh, A., and Hayden, R., "Aerodynamic Sound Radiation from Lifting Surfaces with and Without Leading-Edge Serrations," NASA TR NASA-CR-114370, 1971, https://ntrs.nasa.gov/api/citations/19710 026946/downloads/19710026946.pdf.
- [61] Tam, C., "Discrete Tones of Isolated Airfoils," *Journal of the Acoustical Society of America*, Vol. 55, No. 6, 1974, pp. 1173–1177. https://doi.org/10.1121/1.1914682
- [62] Marsden, A., Wang, M., Mohammadi, B., and Moin, P., "Shape Optimization for Aerodynamic Noise Control," Center for Turbulence Research Annual Brief, 2001, pp. 241–247.
- [63] Marsden, A., Wang, M., Koumoutsakos, P., and Moin, P., "Optimal Aeroacoustic Shape Design Using Approximation Modeling," Center for Turbulence Research Annual Research Briefs 2002, Vol. 201, 2002, p. 213.
- [64] Marsden, A., Wang, M., Dennis, J., and Moin, P., "Optimal Aeroacoustic Shape Design Using the Surrogate Management Framework," *Optimization and Engineering*, Vol. 5, No. 2, 2004, pp. 235–262. https://doi.org/10.1023/B:OPTE.0000033376.89159.65
- [65] Jouhaud, J., Sagaut, P., Montagnac, M., and Laurenceau, J., "A Surrogate-Model Based Multidisciplinary Shape Optimization Method with Application to a 2D Subsonic Airfoil," *Computers & Fluids*, Vol. 36, No. 3, 2007, pp. 520–529. https://doi.org/10.1016/j.compfluid.2006.04.001
- [66] Ikeda, T., and Atobe, T., "Numerical Studies of Acoustic Effects on 2D Airfoil Aerodynamics at a Low Reynolds Number," 50th AIAA Aerospace Sciences Meeting Including the New Horizons Forum and Aerospace Exposition, AIAA Paper 2012-0700, 2012. https://doi.org/10.2514/6.2012-700
- [67] Vermeire, B., "Paired Explicit Runge-Kutta Schemes for Stiff Systems of Equations," *Journal of Computational Physics*, Vol. 393, Sept. 2019, pp. 465–483. https://doi.org/10.1016/j.jcp.2019.05.014
- [68] Vermeire, B., "Embedded Paired Explicit Runge-Kutta Schemes," Journal of Computational Physics, Vol. 487, Aug. 2023, Paper 112159. https://doi.org/10.1016/j.jcp.2023.112159
- [69] Caros, L., Buxton, O., and Vincent, P., "Optimization of Triangular Airfoils for Martian Helicopters Using Direct Numerical Simulations," AIAA Journal, Vol. 61, No. 11, 2023, pp. 4935–4945. https://doi.org/10.2514/1.J063164
- [70] Tugnoli, M., Abbà, A., Bonaventura, L., and Restelli, M., "A Locally p-Adaptive Approach for Large Eddy Simulation of Compressible Flows in a DG Framework," *Journal of Computational Physics*, Vol. 349, Nov. 2017, pp. 33–58. https://doi.org/10.1016/j.jcp.2017.08.007
- [71] Hedayati Nasab, S., Pereira, C. A., and Vermeire, B. C., "Optimal Runge-Kutta Stability Polynomials for Multidimensional High-Order Methods," *Journal of Scientific Computing*, Vol. 89, No. 1, 2021, p. 11. https://doi.org/10.1007/s10915-021-01620-x

P. G. Tucker Associate Editor